High-Fidelity Ion State Detection Using Trap-Integrated Avalanche Photodiodes

David Reens, Michael Collins, Joseph Ciampi, Dave Kharas, Brian F. Aull, Kevan Donlon, Colin D. Bruzewicz, Bradley Felton, Jules Stuart, Robert J. Niffenegger, Philip Rich, Danielle Braje, Kevin K. Ryu, John Chiaverini, and Robert McConnell

Phys. Rev. Lett. **129**, 100502 — Published 2 September 2022

DOI: 10.1103/PhysRevLett.129.100502

High-Fidelity Ion State Detection Using Trap-Integrated Avalanche Photodiodes

David Reens,[1,*] Michael Collins,[1] Joseph Ciampi,[1] Dave Kharas,[1] Brian F. Aull,[1] Kevan Donlon,[1] Colin D. Bruzewicz,[1] Bradley Felton,[1] Jules Stuart,[1,2,†] Robert J. Niffenegger,[1,‡] Philip Rich,[1,2] Danielle Braje,[1] Kevin K. Ryu,[1] John Chiaverini,[1,2] and Robert McConnell[1,§]

[1] *Lincoln Laboratory, Massachusetts Institute of Technology, Lexington, Massachusetts 02421, USA*
[2] *Massachusetts Institute of Technology, Cambridge, Massachusetts 02139, USA*

(Dated: July 14, 2022)

Integrated technologies greatly enhance the prospects for practical quantum information processing and sensing devices based on trapped ions. High-speed and high-fidelity ion state readout is critical for any such application. Integrated detectors offer significant advantages for system portability and can also greatly facilitate parallel operations if a separate detector can be incorporated at each ion-trapping location. Here we demonstrate ion quantum state detection at room temperature utilizing single-photon avalanche diodes (SPADs) integrated directly into the substrate of silicon ion trapping chips. We detect the state of a trapped Sr^+ ion via fluorescence collection with the SPAD, achieving 99.92(1)% average fidelity in 450 µs, opening the door to the application of integrated state detection to quantum computing and sensing utilizing arrays of trapped ions.

Trapped ions are a promising technology for scalable quantum information processing [1, 2] and currently form the basis of the highest-accuracy optical atomic clocks [3]. Integrating elements of these systems may prove essential for scaling quantum information processors, as well as for reducing the size of optical clocks and other quantum sensors for many field-based or space-based applications. Recent advances in integrated control technologies, including photonics for on-chip light delivery [4–7] and electronic control [8], highlight the possibility for a dramatic reduction in the hardware overhead for these systems by performing many ion control functions within the substrate of a surface-electrode ion trap.

Integrating ion detection functions into the trap offers a possibility to reduce system size and complexity by eliminating external lens systems and cameras or photomultiplier tubes typically used for fluorescence-based ion state detection, while also allowing for site-specific readout of a large number of ions. Steps towards this goal have been taken via the use of light-collecting optical fibers [9–11] or optical cavities [12] located within the ion-trapping vacuum system, reflective traps [13, 14], or chip-integrated optics [15–18] for light collection, though in all of these cases a separate photon detector was required outside of the vacuum chamber. A first demonstration of integrated ion detection involved a commercial photodiode attached to a transparent ion trap [19], although only clouds of ∼50 ions could be detected, and the detector size posed an obstacle to further miniaturization. Recently, a superconducting nanowire single-photon detector (SNSPD) was used to detect the state of a single $^9Be^+$ ion in a trap operating at 3.7 K [20], while an integrated avalanche photodiode (APD) detected the presence/absence of a $^{174}Yb^+$ ion in 7.7 ms at room temperature [21]. Nonetheless, rapid, room-temperature, on-chip quantum-state detection of an ion has yet to be achieved.

We here report the rapid and high-fidelity state detection of Sr^+ ions with an efficient, low-dark-current silicon Geiger-mode APD integrated into a surface-electrode ion trap operating at room temperature. In Geiger mode, the APD is biased beyond its breakdown voltage and individual ion fluorescence photons trigger avalanche breakdowns within the APD, generating voltage pulses that can be counted with an external readout circuit; such an APD is referred to as a single-photon avalanche diode (SPAD). A dual-layer transparent conductive indium-tin-oxide (ITO) coating on the trap protects the ion from voltage perturbations due to the pulsing SPAD, allowing stable trapping and coherent operations. We achieve state detection fidelity of 99.92(1)% using a maximum-likelihood estimation technique, in an average detect time of 450 µs with an adaptive scheme. We perform coherent ion quantum operations above the pulsing SPAD and measure an ion motional heating rate of 10 q/ms, which may be improved in the future with better micromotion compensation or surface treatments. The SPAD fabrication is compatible with integrated multi-wavelength photonics processes [5], and thus provides a pathway for the elimination of all free-space optics required for ion trapping and control.

Figure 1(a) shows a simplified level structure of the Sr^+ ion. We store quantum information in the optical clock/qubit states, the ground $|5S_{1/2}, m_J = -1/2\rangle$ and the metastable $|4D_{5/2}, m_J = -5/2\rangle$ state (lifetime 390 ms [22]), which can be coherently coupled via a 674-nm laser. A 422-nm laser is used for Doppler cooling on the broad $5S_{1/2} \rightarrow 5P_{1/2}$ transition. This transition is also used, during readout, to produce fluorescence photons from an ion in the ground state; because the 422-nm laser does not couple to the $4D_{5/2}$ state, the latter will appear dark, thus allowing discrimination between the bright $5S_{1/2}$ and dark $4D_{5/2}$ state. Additional lasers at 1033 nm and 1092 nm are used for quenching of the metastable state and for pumping out of the undesired $4D_{3/2}$ state, respectively.

Figure 1(b) shows a cross-sectional view of the fab-

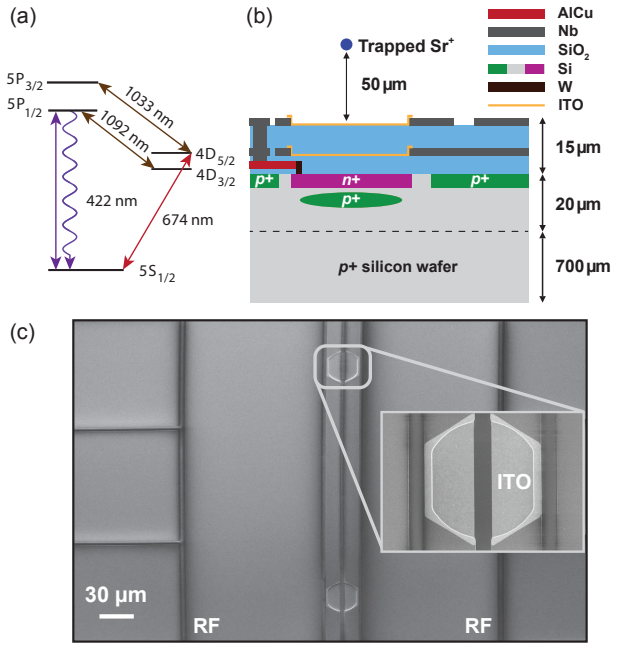

FIG. 1. (a) Simplified level structure of the Sr^+ion. (b) Cross-sectional illustration of the fabricated SPADs within the ion trap chip (not to scale). (c) SEM image of representative device after fabrication (plan view). SPADs with ITO coating (seen in inset) are located directly underneath ion trapping sites and spaced 240 µm apart. RF voltage is applied to the two indicated electrodes, while DC voltages are applied to the remaining electrodes to generate an ion-trapping potential as described in the text.

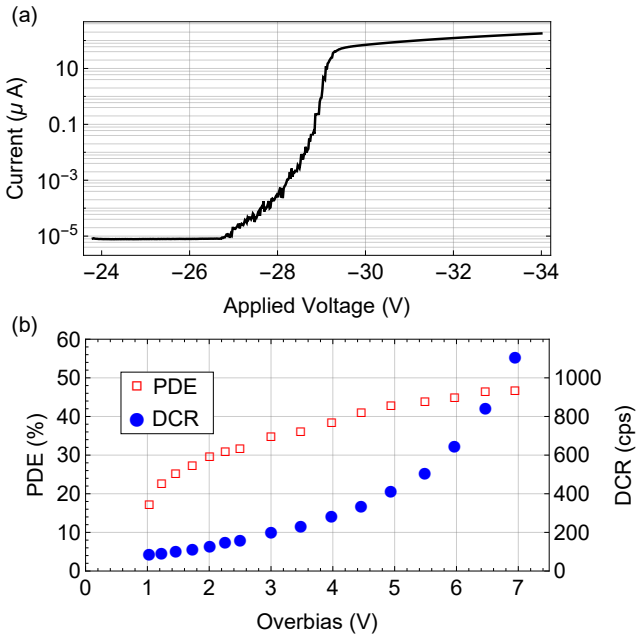

FIG. 2. Measured SPAD characteristics. (a) Current vs. voltage curve of a representative device, indicating breakdown voltage near −28 V; the measurement is taken with a current limit of 200 µA. (b) External photon detection efficiency (PDE, red squares) at wavelength of 420 nm and device dark count rate (DCR, blue circles) of a representative device as a function of device overbias. Error bars are comparable to the point size.

ricated ion traps with integrated SPADs. SPADs are fabricated on a p-type Si wafer and are optimized for performance at 422 nm, but could also be used for detection at other visible wavelengths. Details of SPAD fabrication can be found in the Supplemental Material [23]. After SPADs were fabricated and tested, a Nb metal ground plane was deposited on top of a 2-µm-thick oxide layer, with apertures to allow electrical connections and optical access to the SPADs. A second, 10-μm-thick oxide layer was then added, followed by patterned Nb electrode metal to form a linear surface-electrode Paul trap [24]. SPADs are located directly under seven ion-trapping sites on the 1 cm × 1 cm trap. The diameter of each SPAD's photo-sensitive region is 40 µm, but ion trap electrodes obscure a portion of the SPAD active area and result in a 30-µm-diameter clear aperture (Fig. 1(b)). Two layers of ITO were used, one over the SPAD aperture in the ground plane and one over the similar aperture in the trap metal, to shield the ion from SPAD pulses and to shield the SPAD from trap radio frequency (RF) voltage (∼ 50 V amplitude). A scanning-electron microscope (SEM) image of the finished devices is shown in Fig. 1(c).

We characterized the SPADs' current-voltage characteristic, external photon detection efficiency (PDE) at the ion fluorescence wavelength of 422 nm, and dark count rate (DCR). The PDE was measured using a time-to-first-pulse method [23] to avoid overestimating SPAD efficiency due to afterpulsing effects. Fig. 2 shows measurements of these parameters for a typical SPAD from the same wafer, and of the same design, as the device used for ion-trap measurements. Panel (a) shows SPAD current versus applied voltage while in darkness, indicating a breakdown voltage of approximately −28 V, while panel (b) shows the PDE and DCR versus excess reverse bias relative to this breakdown voltage (overbias). The device we use for ion detection measurements exhibits a DCR of 109 ± 2 counts per second (cps) and PDE of 25.2(2)% at 2 V overbias, both slightly below the values obtained from the measurement in panel (b) but consistent with typical device-to-device variation.

To characterize ion-detection performance of the integrated SPAD trap, we install one of these traps into a room-temperature ion-trapping system [23]. Briefly, we trap single $^{88}Sr^+$ ions 50 µm above the trap with typical axial frequency of $2\pi \times 700$ kHz and radial frequencies of $\sim 2\pi \times 5$ MHz. The experiments described in this work were primarily performed over a single SPAD on the trap, but we observed similar performance when trapping and detecting an ion over a second device on this same trap.

The trap-integrated SPAD is read out using a passive quenching circuit [23], with a ∼500 ns quench time and 3.5 µs recharge time ($1/e$ times). Optimum performance,

taking into account speed limitations due to readout-circuit capacitance, is obtained with a 2 V overbias for a total count rate 106 kcps (38 kcps) while detecting the bright (dark) ion state, with background counts dominated by laser scatter from the 422-nm detection and 1092-nm repump beams.

We define ion state detection fidelity as $F = 1 - (\epsilon_{\text{bright}} + \epsilon_{\text{dark}})/2$, with ϵ_i the detection error when the ion is in state i. To avoid the necessity of high-fidelity dark state preparation, we prepare the ion in a nearly-equal superposition of bright and dark states via a $\pi/2$ pulse on the $5S_{1/2} \rightarrow 4D_{5/2}$ transition. We perform detection simultaneously with the integrated SPAD and with a high NA lens focused onto a photomultiplier tube (PMT) located outside of the vacuum chamber. As the PMT is far less susceptible to laser scatter due to its distance from the detection beams and to spatial and spectral filtering provided by the high-NA lens and a 422-nm bandpass optical filter, we use it as a reference against which to compare the SPAD. We determine the SPAD error rates ϵ_{bright} and ϵ_{dark} from the discrepancy between SPAD and PMT state identification and average to find the mean infidelity, taking into account the PMT detection error separately as described below. Detection data are binned at 25 μs intervals and post-processed to determine readout error as a function of detection time (see Fig. 3).

Discrimination between the bright and dark states can be performed in multiple ways. The most straightforward establishes a threshold of counts in a given time—based on the observed bright and dark count rates from the ion—with the ion being assigned to the bright (dark) state if counts exceed (do not exceed) the threshold. Simple thresholding in our system achieves $F = 99.89(1)\%$ in 950 µs with a threshold of 66.5 counts; the prepared superposition is found to project to the bright state in 49.8% of trials. A readout method utilizing more information is maximum likelihood estimation [25], which compares the probabilities of the observed count distributions for bright and dark ions via an iterative algorithm. Maximum-likelihood estimation deals better with those instances in which the metastable dark state decays during measurement and achieves $F = 99.92(1)\%$ in 1.2 ms in our system. Detection speed can be improved with an adaptive readout scheme [25], which is similar to the maximum-likelihood method but concludes measurement when the expected probability of a correct detection exceeds a user-specified threshold. We implement an adaptive readout scheme via post-processing of our SPAD data. The adaptive readout also reaches $F = 99.92\%$, but in an average detection time of 450 µs. The time required for adaptive detection is primarily limited by scatter from the detection beams. We estimate that if stray light could be eliminated, adaptive detection could achieve $F = 99.9\%$ in 75 µs , or $F = 99.98\%$ in 125 µs, given the characteristics of our SPAD and biasing circuit.

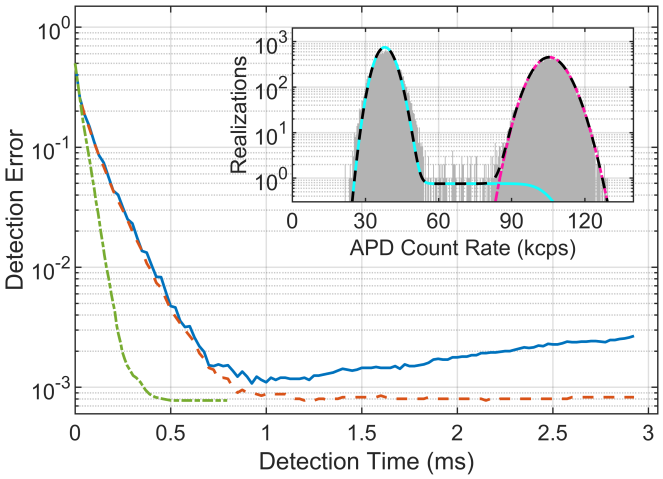

FIG. 3. State detection error for simple thresholding (blue), maximum likelihood analysis (red dashed), and using an adaptive readout scheme (green dash dot). Inset: Histogram of counts recorded by SPAD in 40,000 ion state-detection trials with detection time of 2.9 ms. The fit (black dashed) is the weighted sum of a bright-state Poisson distribution (pink), and a dark-state distribution (cyan) that includes a plateau corresponding to metastable decay during measurement. The dark state distribution exhibits slightly increased variance relative to the Poissonian expectation, which is accounted for during likelihood estimation [23].

Our fidelity measurements must take into account the possibility of an error when using the PMT to determine ion state. We minimize expected PMT errors by using a maximum likelihood detection process similar to what we use for the SPAD. The PMT has an expected error rate of $\epsilon_{\text{PMT}} = 3.5 \pm 0.1 \times 10^{-4}$, obtained by simulating the maximum likelihood process including metastable decay. The PMT error is dominated by instances when the dark-state ion decays very early during the measurement, such that insufficient time is available to distinguish between the bright and dark ion states. In these instances, simulations suggest that the SPAD is at least 90% likely to also incorrectly detect the state. Because of this correlation of SPAD and PMT errors, we conservatively assume that all PMT errors give rise to SPAD errors. The SPAD detection error $(1 - F)$ shown in Fig. 3 and throughout this work is thus the sum of the measured rate of disagreement between the SPAD and PMT and the estimated PMT error ϵ_{PMT}.

Low optical and electronic crosstalk between different detectors in an on-chip array will be required if they are to be used in larger sensing or information processing ensembles. To characterize potential optical crosstalk in a SPAD array, we measured the dependence of the SPAD count rate as the ion trapping location was translated along the axial direction away from the SPAD. For these measurements, we prepare a superposition state as described previously, use the PMT to determine the state of the ion, and subtract the average SPAD background

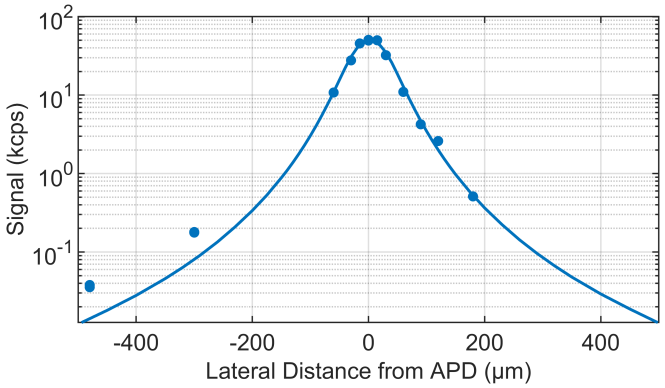

FIG. 4. Measured counts from the SPAD as a function of ion lateral distance from SPAD center. The model line accounts for the full geometry and for reflection and refraction at dielectric interfaces between the trap surface and the SPAD. Statistical error bars are smaller than the size of the markers.

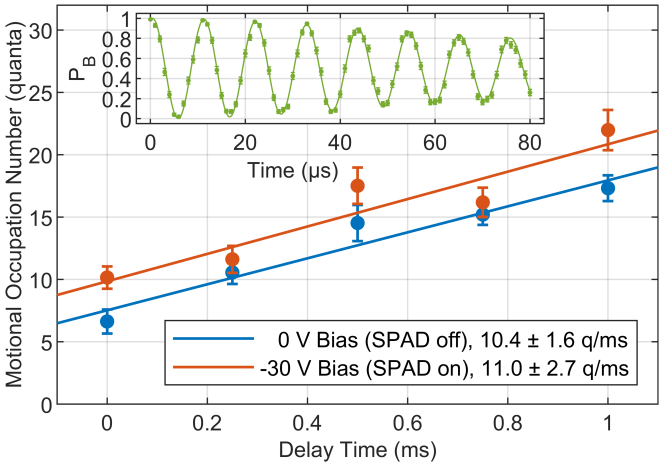

FIG. 5. Occupation numbers of a radial motional mode with $\omega = 2\pi \times 5\,\mathrm{MHz}$ are measured after varying delays, with the SPAD either off or on, and data collected with an external PMT. Lines are linear fits with resulting heating rates given in the legend. Inset: Rabi oscillations on the $5S_{1/2} \rightarrow D_{5/2}$ transition are fitted to obtain the average motional occupation number for each delay. The data and fit shown here correspond to $\bar{n} = 6.3 \pm 0.3$ quanta, and Rabi frequency $\Omega = 2\pi \times 94.7 \pm 0.1\,\mathrm{kHz}$. P_B: Bright state probability.

count rate from the average bright-ion count rate. The count rate for ions directly above the SPAD is 60 kcps, which declines to only 0.18 kcps at a lateral distance of 300 μm and to 0.037 kcps at a distance of 480 μm. At smaller values of ion-SPAD distance, the count rate is found to obey a ray-tracing model accounting for full geometry (Fig. 4) including reflections and refractions at the dielectric interfaces between the trap surface and the SPAD. The discrepancy between model and experiment at larger distances seen in Fig. 4 may be attributable to light which passes through gaps between trap electrodes and becomes confined in the oxide layer separating the metal ground plane from the electrodes (Fig 1b), eventually reaching the SPAD. Nevertheless, the results suggest that, for ion array site spacings greater than 300 μm, additional background counts due to optical crosstalk would have a negligible effect on detection given the 38 kcps laser scatter rate. If all stray light were to be eliminated, optical crosstalk from an adjacent device would not prohibit us from reaching 99.98% fidelity (the best achievable given this device's PDE and DCR) and would only increase the time required to do so from 125 μs to 140 μs.

We additionally perform a measurement to detect electronic crosstalk between SPADs, by trapping an ion above one SPAD, detecting with a SPAD 480 μm away, and enabling or disabling the readout circuit for the first SPAD. Biasing the SPAD below the ion reduces the count rate of the distant SPAD by 40 ± 20 cps, an amount small compared to the 68 kcps count rate induced by a bright ion. This effect, which is likely due to a slight reduction in the common bias voltage shared by the SPADs, does not pose an obstacle to reading out moderate-scale SPAD arrays with this spacing, and could be further mitigated by improving bias stiffness.

In order to be useful for quantum information processing or sensing purposes, integrated detectors must be compatible with high-fidelity quantum control of trapped ions. We demonstrate quantum control of the ion above the pulsing SPAD by performing Rabi oscillations via the 674-nm beam. Fig. 5(inset) shows a typical Rabi oscillation with 5 μs π-pulse time and fitted contrast of 99.8%, limited by the ion's initial Doppler-cooled temperature.

The motional heating rate experienced by ions close to the SPAD is a key figure of merit for the compatibility of the device with the coherent operations required for atomic clocks or quantum computations. We measure the heating of a radial mode with frequency $\omega = 2\pi \times 5\,\mathrm{MHz}$ by fitting the decay of contrast seen in Rabi spectroscopy of the metastable-state carrier transition as a function of delay time. We note that, during installation of this trap, some wirebonds to electrodes near the trapped ion's location detached, making full elimination of the ion's excess micromotion difficult. After optimizing the ion's electric-field compensation with the remaining electrodes to minimize the ion's initial average motional excitation $\bar{n}$, we obtain heating rates of approximately 10 quanta/ms directly above the SPAD (Fig. 5). We find that the observed heating rate does not depend on SPAD bias voltage within our margin of error.

The observed heating rate is high compared to that measured at 295 K for Nb ion traps of similar electrode configuration [26]. Because of the difficulty in minimizing micromotion in this trap, it is difficult to unambiguously determine the cause of the higher heating rate in this system. We observe rates as low as 0.5 quanta/ms at a distance 60 μm away from the SPAD, potentially implicating the SPAD or ITO. Future investigations may be able to more fully characterize the heating rate over the SPAD, and adapted processing or surface modification, such as surface milling by Ar ions [26–28], could be effec-

tive in reducing it.

In summary, we have demonstrated rapid and high-fidelity ion state detection with a chip-integrated SPAD, achieving 99.92(1)% detection fidelity in 450 µs with an adaptive technique. The demonstrated SPAD performance lends itself to on-chip, site-specific detection of arrays of ions for optical clocks or quantum information processing purposes. We also demonstrate low levels of optical and electrical crosstalk between multiple SPADs on the chip separated by hundreds of microns, particularly relevant for optical clocks (where clock ions may be individually trapped and do not necessarily need to be entangled), or for a quantum computing architecture in which ions are shuttled between different sites for entangling and readout operations [29, 30]. These SPADs may also be used in on-chip remote-entanglement generation if light collected from two or more ions can be routed through an integrated beamsplitter to SPADs such that "which-path" information is removed.

The currently achieved fidelity is limited by scattered light from the measurement and repumping lasers; if eliminated, infidelities and detect times could be reduced four-fold. We note that state-of-the-art for high-fidelity, rapid ion state detection is 99.991% in 145 µs [25], and detection times as low as 10 µs have been achieved with lower fidelity [31]; elimination of background counts due to stray laser light in our experiment could allow us to approach that fidelity and potentially achieve sub-100-µs detection times. As more ion-control components—particularly integrated photonics—begin to be incorporated into surface-electrode traps, it will be necessary to carefully screen out any light scattered by on-chip components to prevent overwhelming integrated single-photon detectors. Further improvements in detection time and fidelity might be achieved with an active quenching system, reducing the recovery time of the SPAD at the expense of additional experimental complexity. We briefly note that we have tested these SPADs at cryogenic temperature and found them to operate, but with a roughly two-orders-of-magnitude lower PDE, precluding rapid ion-state detection. Future work may focus on SPADs optimized for cryogenic temperatures and on reducing the observed ion motional heating rate near the SPAD via surface treatments or low-temperature operation.

We thank S. L. Todaro for helpful manuscript comments, M. Purcell-Schuldt for trap layout, and P. Murphy and C. Thoummaraj for chip packaging. This material is based upon work supported by the Defense Advanced Research Projects Agency under Air Force Contract No. FA8702-15-D-0001 and by the U.S Department of Energy, Office of Science, National Quantum Information Science Research Centers, Quantum Systems Accelerator. Any opinions, findings, conclusions or recommendations expressed in this material are those of the author(s) and do not necessarily reflect the views of the Defense Advanced Research Projects Agency or the Department of Energy.

* david.reens@ll.mit.edu
† Present address: National Institute of Standards and Technology, Boulder, CO
‡ Present address: University of Massachusetts-Amherst, Amherst, MA
§ robert.mcconnell@ll.mit.edu

[1] H. Haffner, C. Roos, and R. Blatt, Physics Reports **469**, 155 (2008).
[2] C. D. Bruzewicz, J. Chiaverini, R. McConnell, and J. M. Sage, Applied Physics Reviews **6**, 021314 (2019).
[3] S. M. Brewer, J. S. Chen, A. M. Hankin, E. R. Clements, C. W. Chou, D. J. Wineland, D. B. Hume, and D. R. Leibrandt, Phys. Rev. Lett. **123**, 033201 (2019).
[4] K. K. Mehta, C. D. Bruzewicz, R. McConnell, R. J. Ram, J. M. Sage, and J. Chiaverini, Nature Nanotechnology **11**, 1066 (2016).
[5] R. J. Niffenegger, J. Stuart, C. Sorace-Agaskar, D. Kharas, S. Bramhavar, C. D. Bruzewicz, W. Loh, R. T. Maxson, R. McConnell, D. Reens, G. N. West, J. M. Sage, and J. Chiaverini, Nature **586**, 538 (2020).
[6] K. K. Mehta, C. Zhang, M. Malinowski, T.-L. Nguyen, M. Stadler, and J. P. Home, Nature **586**, 533 (2020).
[7] M. Ivory, W. J. Setzer, N. Karl, H. McGuinness, C. DeRose, M. Blain, D. Stick, M. Gehl, and L. P. Parazzoli, Phys. Rev. X **11**, 041033 (2021).
[8] J. Stuart, R. Panock, C. Bruzewicz, J. Sedlacek, R. McConnell, I. Chuang, J. Sage, and J. Chiaverini, Phys. Rev. Applied **11**, 024010 (2019).
[9] A. P. VanDevender, Y. Colombe, J. Amini, D. Leibfried, and D. J. Wineland, Phys. Rev. Lett. **105**, 023001 (2010).
[10] H. Takahashi, A. Wilson, A. Riley-Watson, F. Oručević, N. Seymour-Smith, M. Keller, and W. Lange, New Journal of Physics **15**, 053011 (2013).
[11] C. R. Clark, C.-W. Chou, A. R. Ellis, J. Hunker, S. A. Kemme, P. Maunz, B. Tabakov, C. Tigges, and D. L. Stick, Phys. Rev. Applied **1**, 024004 (2014).
[12] J. D. Sterk, L. Luo, T. A. Manning, P. Maunz, and C. Monroe, Phys. Rev. A **85**, 062308 (2012).
[13] P. F. Herskind, S. X. Wang, M. Shi, Y. Ge, M. Cetina, and I. L. Chuang, Opt. Lett. **36**, 3045 (2011).
[14] A. Van Rynbach, P. Maunz, and J. Kim, Applied Physics Letters **109**, 221108 (2016).
[15] J. T. Merrill, C. Volin, D. Landgren, J. M. Amini, K. Wright, S. C. Doret, C.-S. Pai, H. Hayden, T. Killian, D. Faircloth, K. R. Brown, A. W. Harter, and R. E. Slusher, New Journal of Physics **13**, 103005 (2011).
[16] A. Jechow, E. W. Streed, B. G. Norton, M. J. Petrasiunas, and D. Kielpinski, Opt. Lett. **36**, 1371 (2011).
[17] E. W. Streed, B. G. Norton, A. Jechow, T. J. Weinhold, and D. Kielpinski, Phys. Rev. Lett. **106**, 010502 (2011).
[18] M. Ghadimi, V. Blüms, B. G. Norton, P. M. Fisher, S. C. Connell, J. M. Amini, C. Volin, H. Hayden, C.-S. Pai, D. Kielpinski, M. Lobino, and E. W. Streed, npj Quantum Information **3**, 4 (2017).
[19] A. M. Eltony, S. X. Wang, G. M. Akselrod, P. F. Herskind, and I. L. Chuang, Applied Physics Letters **102**, 054106 (2013).
[20] S. L. Todaro, V. B. Verma, K. C. McCormick, D. T. C.

Allcock, R. P. Mirin, D. J. Wineland, S. W. Nam, A. C. Wilson, D. Leibfried, and D. H. Slichter, Phys. Rev. Lett. **126**, 010501 (2021).
[21] W. J. Setzer, M. Ivory, O. Slobodyan, J. W. Van Der Wall, L. P. Parazzoli, D. Stick, M. Gehl, M. G. Blain, R. R. Kay, and H. J. McGuinness, Applied Physics Letters **119**, 154002 (2021).
[22] U. Safronova and M. Safronova, Canadian Journal of Physics **89**, 465 (2011).
[23] See Supplementary Materials for more detailed information on SPAD fabrication, time-to-first-pulse method for measuring device eficiency, ion trap apparatus and quenching circuit, contributions to the background count rate, and accounting for overdispersion in the fluorescence distribution. Refs. [32–35] are included as well.
[24] J. Chiaverini, R. B. Blakestad, J. Britton, J. D. Jost, C. Langer, D. Leibfried, R. Ozeri, and D. J. Wineland, Quant. Inf. Comp. **5**, 419 (2005).
[25] A. H. Myerson, D. J. Szwer, S. C. Webster, D. T. C. Allcock, M. J. Curtis, G. Imreh, J. A. Sherman, D. N. Stacey, A. M. Steane, and D. M. Lucas, Phys. Rev. Lett. **100**, 200502 (2008).
[26] J. A. Sedlacek, J. Stuart, D. H. Slichter, C. D. Bruzewicz, R. McConnell, J. M. Sage, and J. Chiaverini, Phys. Rev. A **98**, 063430 (2018).
[27] D. A. Hite, Y. Colombe, A. C. Wilson, K. R. Brown, U. Warring, R. Jördens, J. D. Jost, K. S. McKay, D. P. Pappas, D. Leibfried, and D. J. Wineland, Phys. Rev. Lett. **109**, 103001 (2012).
[28] N. Daniilidis, S. Gerber, G. Bolloten, M. Ramm, A. Ransford, E. Ulin-Avila, I. Talukdar, and H. Häffner, Phys. Rev. B **89**, 245435 (2014).
[29] D. Wineland, C. Monroe, W. M. Itano, D. Leibfried, B. E. King, and D. M. Meekhof, J. Res. Natl Inst. Stand. Technol. **103**, 259 (1998).
[30] D. Kielpinski, C. Monroe, and D. J. Wineland, Nature **417**, 709 (2002).
[31] R. Noek, G. Vrijsen, D. Gaultney, E. Mount, T. Kim, P. Maunz, and J. Kim, Opt. Lett. **38**, 4735 (2013).
[32] M. Green and M. Keevers, Prog. Photovolt.: Res. Appl. **3**, 189 (1995).
[33] W. Oldham, R. Samuelson, and P. Antognetti, IEEE Transactions on Electron Devices **19**, 1056 (1972).
[34] B. F. Aull, Optical Sensing, Imaging and Photon Counting: From X-Rays to THz **10729**, 20 (2018).
[35] A. Gelman, J. B. Carlin, H. S. Stern, and D. B. Rubin, *Bayesian Data Analysis* (Chapman and Hall/CRC, Boca Raton, FL, 2004) pp. 446–447.